



**HAL**  
open science

# Passive seismic imaging with directive ambient noise: application to surface waves and the San Andreas Fault in Parkfield, CA

Philippe Roux

► **To cite this version:**

Philippe Roux. Passive seismic imaging with directive ambient noise: application to surface waves and the San Andreas Fault in Parkfield, CA. *Geophysical Journal International*, 2018, 179 (1), pp.367 - 373. 10.1111/j.1365-246x.2009.04282.x . hal-04028152

**HAL Id: hal-04028152**

**<https://hal.science/hal-04028152>**

Submitted on 14 Mar 2023

**HAL** is a multi-disciplinary open access archive for the deposit and dissemination of scientific research documents, whether they are published or not. The documents may come from teaching and research institutions in France or abroad, or from public or private research centers.

L'archive ouverte pluridisciplinaire **HAL**, est destinée au dépôt et à la diffusion de documents scientifiques de niveau recherche, publiés ou non, émanant des établissements d'enseignement et de recherche français ou étrangers, des laboratoires publics ou privés.

See discussions, stats, and author profiles for this publication at: <https://www.researchgate.net/publication/215754750>

# Passive seismic imaging with directive ambient noise: application to surface waves and the San Andreas Fault in Parkfield, CA

Article in *Geophysical Journal International* · October 2009

DOI: 10.1111/j.1365-246X.2009.04282.x

CITATIONS

94

READS

407

1 author:



Philippe Roux

University Grenoble Alpes

494 PUBLICATIONS 13,002 CITATIONS

SEE PROFILE

Some of the authors of this publication are also working on these related projects:



Advanced array processing in the geophysics exploration context [View project](#)



Ocean acoustic tomography in shallow water [View project](#)

# Passive seismic imaging with directive ambient noise: application to surface waves and the San Andreas Fault in Parkfield, CA

Philippe Roux

LGIT, CNRS UMR 5559, Université Joseph Fourier, Grenoble, France. E-mail: philippe.roux@obs.ujf-grenoble.fr

Accepted 2009 June 3. Received 2009 June 3; in original form 2009 April 2

## SUMMARY

This study deals with surface waves extracted from microseismic noise in the (0.1–0.2 Hz) frequency band with passive seismic-correlation techniques. For directive noise, we explore the concept of passive seismic-noise tomography performed on three-component sensors from a dense seismic network. From the nine-component correlation tensor, a rotation algorithm is introduced that forces each station pair to re-align in the noise direction, a necessary condition to extract unbiased traveltime from passive seismic processing. After rotation is performed, the new correlation tensor exhibits a surface wave tensor from which Rayleigh and Love waves can be separately extracted for tomography inversion. Methodological aspects are presented and illustrated with group-speed maps for Rayleigh and Love waves and ellipticity measurements made on the San Andreas Fault in the Parkfield area, California, USA.

**Key words:** Time series analysis; Interferometry; Surface waves and free oscillations; Seismic tomography; Wave propagation.

## INTRODUCTION

Passive seismic tomography is based on the extraction of the surface wave contribution to the seismic field from the cross-correlation of seismic noise between station pairs (Sabra *et al.* 2005a; Shapiro *et al.* 2005). As described in many studies where noise has been used to obtain the Green's function between receivers, surface waves are extracted from noise signals that remain coherent even if, at first sight, this coherent signal appears deeply buried in the local incoherent seismic noise.

Recent studies on passive seismic processing have focused on two applications, the noise-extracted Green's functions associated to Rayleigh waves leads to subsurface imaging on scales ranging from thousands of kilometres (Yang *et al.* 2007) to very short distances (Picozzi *et al.* 2009); on the other hand, even when the Green's function is not satisfactorily reconstructed from seismic ambient noise, it has been shown that seismic monitoring is feasible using the scattered waves of the noise-correlation function (Brenquier *et al.* 2008a, 2008b). In both cases, the quality of the results strongly depends on: (1) the spatial-temporal properties of the noise source distribution and (2) the number of seismic receiver pairs on which the noise correlation is performed.

For seismic waves, it has been shown theoretically that the convergence of noise correlation to the Green's function is bonded by the equipartition condition of the different components of the elastic field (Sánchez-Sesma & Campillo 2006). In other words, the emergence of the Green's function is effective after a sufficient self-averaging process that is provided by the random spatial distribution of the noise sources, when considering long time-series as well as scattering (Campillo 2006; Larose *et al.* 2006; Gouédard *et al.* 2008).

In practice though, an omni-directional noise source distribution is hard to find in seismology and most studies on passive seismic processing have to deal with a more-or-less directional noise source distribution (Roux *et al.* 2005). In this case, the common practice is to throw away station pairs that do not align with the noise direction, since they provide a biased traveltime through noise correlation. The main objective of this study is to introduce an Optimal Rotation Algorithm (ORA) that allows each station to freely re-align in the incident noise direction whatever the station pair alignment. In this way, we intend to increase the number of station pairs that can be used in the traveltime tomography inversion.

The ORA is based on the continuous recording of seismic noise on three-component sensors. As such, and since passive seismic tomography performs better with large and dense seismic networks, it definitely requires important computing resources. Thus, even if seismic sensors are indeed three component, most studies have been limited so far to noise correlation on vertical components, assuming that information on horizontal components will either be redundant or may suffer from poor signal-to-noise ratios.

In this study, we demonstrate that noise-correlation processing for three-component receivers gives a nine-component surface wave tensor from which it is possible to separate Love and Rayleigh waves, thus providing at least two independent information sources about the seismic medium. We also chose to investigate the difficult case of a directive seismic-noise distribution. From the nine-component correlation tensor measured from each pair of three-component seismometers among the array, the ORA forces each station pair to align along the noise direction. A new surface wave tensor is then obtained that can be used for the tomography goals of both Love and Rayleigh waves. The example of a Rayleigh-wave ellipticity map is also presented for the Parkfield area (CA, USA)

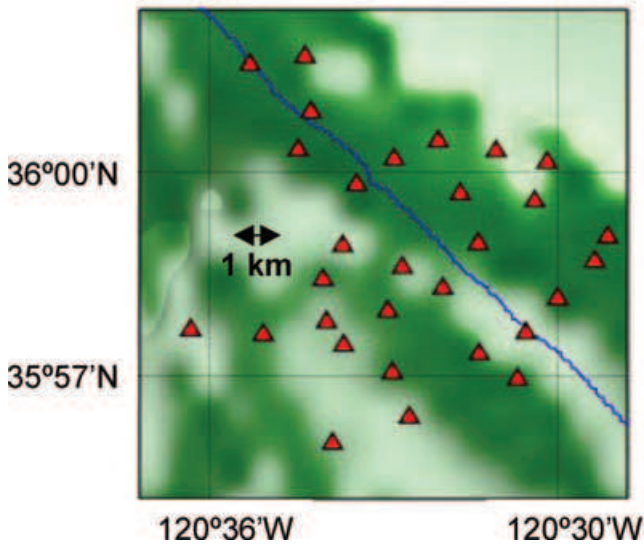


**Figure 1.** Topographic map of the Parkfield area (an 11 km large square; CA, USA) showing the stations (triangles) and the SAF (blue).

using 15 days of continuous seismic noise data that were recorded at 30 broad-band three-component stations located in an area of 11 km<sup>2</sup> (Fig. 1).

## METHODOLOGY

Active tomography was performed from data recorded by a dense seismic network installed in the Parkfield area, California, between 2001 July and 2002 October. This network was extensively used to image the San Andreas Fault (SAF) using man-made explosions and earthquakes (Ben-Zion & Malin 1991; Catchings *et al.* 2002; Thurber *et al.* 2004).

We proposed to revisit the ambient noise data using methodology adapted to passive surface wave tomography. The first two steps (steps 1 and 2) occur before cross-correlating the noise traces, and they consist in noise pre-processing according to the tomography goal. After the noise-correlation tensor is calculated (step 3), an ORA is performed on each station pair, to transform the correlation tensor into a surface wave Green's tensor, including both Rayleigh and Love waves (step 4). From there, a tomography algorithm can be applied that takes into account the effective distance between each station pair according to the ORA (step 5) and the noise direction. Rayleigh wave ellipticity is also extracted from the noise-correlation tensor and clearly exhibits the fractured zone around the SAF (step 6). These six steps are carried out as follows.

*Step 1:* Noise pre-processing consists of eliminating high-amplitude seismic events by truncating the recording amplitude at three times the standard deviation of the seismic noise. Then, equalization is performed to whiten the noise spectrum in the chosen frequency interval (Bensen *et al.* 2007). Some studies have combined these two steps into a simpler 1-bit discretization of the signals (Campillo & Paul 2003; Shapiro *et al.* 2005). The resulting noise-correlation functions are often similar when seismic noise is not dominated by electronic noise, as is always the case in geophysics. However, with regard to our tomography goal, frequency equalization has the advantage of forcing each station to have a similar noise spectrum, thereby avoiding bias in the determination of the traveltimes measurements from the noise-correlation tensor.

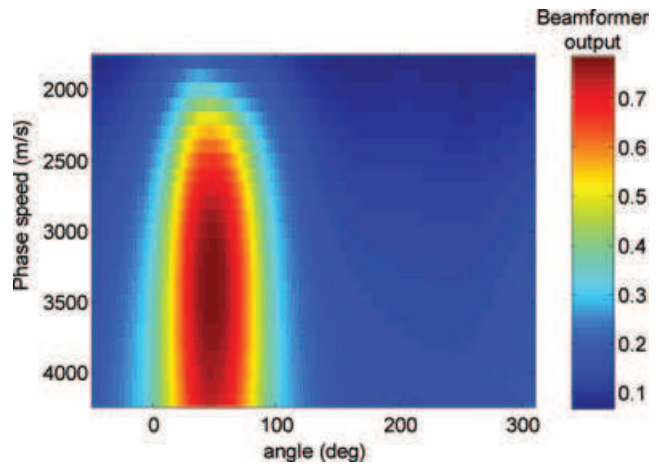


**Figure 2.** Angular-speed distribution of pre-processed incoming noise on the Parkfield network averaged over 1 d. Plane-wave beam-forming is summed incoherently over 100 frequencies from 0.1 to 0.2 Hz. The x-axis corresponds to noise directivity  $\theta_0$  (North is 0°, positive rotation is clockwise), the y-axis to speed  $c$ . Units are arbitrary.

It is important to bear in mind that whatever pre-processing is carried out on the raw ambient noise data, the basic idea behind noise correlation is to work with a spatial and temporal diffuse field. If noise is not Gaussian in time, if strong peaks are still present in the time-domain signal, or if some frequencies dominate, then the requirements to retrieve the Green's function from noise correlation are not fulfilled. The same conditions apply to spatial information, where the noise distribution should be isotropic; this study was designed to work around this condition through the ORA. The pre-processing applied to the raw ambient noise data is always performed to improve the noise properties, such that it behaves as required by the noise correlation theorem (Gouédard *et al.* 2008). In other words, the pre-whitening is generally a must-do processing that changes the natural seismic noise data into a signal to which noise-correlation processing can be applied.

*Step 2:* Frequency-incoherent beamforming is performed using the  $N$  stations of the network ( $N = 30$ ) to determine the average velocity  $c$  and the direction  $\theta$  of the seismic noise (Rost & Thomas 2002; Roux & Kuperman 2004). The beamforming  $B(\theta, c)$  is performed in the bandwidth of interest (0.1–0.2 Hz) on a one-day-long seismic noise data segment

$$B(\theta, c) = \frac{1}{\Delta\omega} \int_{\omega_c - \Delta\omega/2}^{\omega_c + \Delta\omega/2} \left| \sum_{i=1}^N \tilde{S}_i(\omega) \exp \left[ j \frac{\omega}{c} (x_i \sin \theta + y_i \cos \theta) \right] \right|^2 d\omega, \quad (1)$$

where  $\omega_c$  is the central noise frequency and  $\Delta\omega$  the frequency bandwidth,  $\tilde{S}_i(\omega)$  is the complex Fourier component at frequency  $\omega$  of the vertical component  $S_i(t)$  on the  $i$ th seismic station ( $i \in [1, N]$ ), and  $(x_i, y_i)$  are the spatial coordinates of station number  $i$ . Working with a dense seismic network over a small area allows the determination of an average apparent velocity for incident noise using plane-wave beamforming. The noise field clearly originated from the Pacific Ocean ( $\theta_0 \sim 55^\circ$ ; North is 0°, positive rotation is clockwise) and was received on the Parkfield network with an apparent phase velocity  $c \sim 3.2 \text{ km s}^{-1}$  in the frequency bandwidth of interest (Fig. 2).

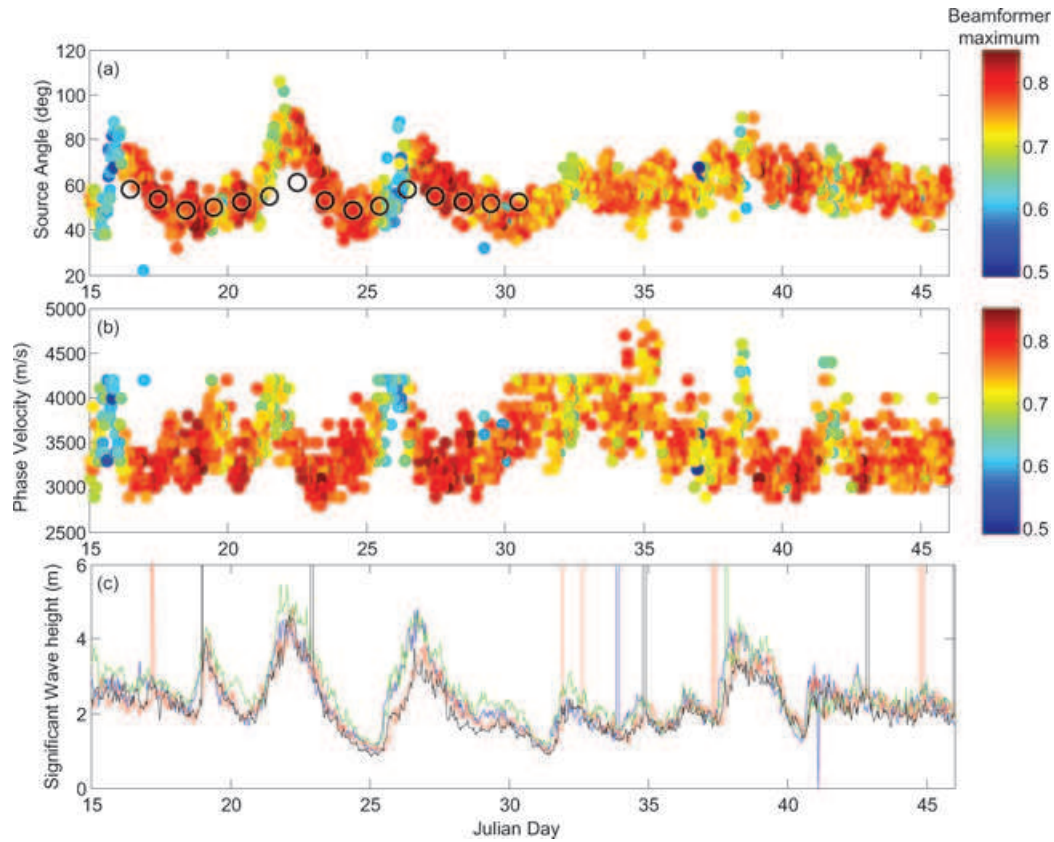


**Figure 3.** Angular (a) and speed (b) representations of the plane-wave beam-former outputs ( $\theta_0, c$ ) (see Fig. 2) applied on 1 hr of incoming noise (with 50 per cent overlap) between 0.1 and 0.2 Hz for 31 consecutive days. The colour scale corresponds to the maximum values of the beam-former. Units are arbitrary. Black circles in (a) correspond to the day-by-day average azimuthal rotation angle obtained from Fig. 5. (c) Significant wave height measured on four wave rider buoys along the Californian coast (from San Diego to Monterey Bay) for the same time period.

Figs 3(a) and (b) shows the time evolution of the beamformer outputs ( $\theta_0, c$ ) for 1-hr-long data segments over 31 consecutive Julian days. The daily fluctuations of  $\theta_0$  correlated with significant wave heights measured along the Californian shore (Fig. 3c), which confirms the oceanic origin of the secondary peak micro-seismic excitation in the (0.1–0.2 Hz) bandwidth (Tanimoto *et al.* 2006).

*Step 3:* The nine-component noise-correlation tensor  $C_{AB}(t)$  is computed for each station pair  $A$  and  $B$  as

$$[C_{AB}(t)]_{ij} = \frac{\int_0^T S_{A,i}(\tau) S_{B,j}(t + \tau) d\tau}{\sqrt{\int_0^T S_{A,i}^2(\tau) d\tau \int_0^T S_{B,j}^2(\tau) d\tau}}, \quad (2)$$

where  $S_{A,i}(t)$  and  $S_{B,i}(t)$  are the vertical ( $i = Z$ ), radial ( $i = R$ ) or transverse ( $i = T$ ) components of the pre-processed noise signals according to station  $A$  and  $B$  locations. For example,  $S_{A,R}(t) = \sin \varphi S_{A,E}(t) + \cos \varphi S_{A,N}(t)$ , where  $S_{A,E}(t)$  and  $S_{A,N}(t)$  are the east and north components of the pre-processed noise field received at station  $A$ ;  $\varphi$  is the angle between stations  $A$  and  $B$ .

The recording time window  $T$  on which the correlation is performed was set to 1 d. The nine components of the noise-correlation tensor were then sorted as  $ZZ, ZR, ZT, RZ, RR, RT, TZ, TR$  and  $TT$  (Fig. 4a, red).

The denominator in eq. (2) is a normalization factor that mitigates local effects and helps in the determination of the actual coherence of the noise field between the stations. Indeed, the autocorrelation  $[C_{AA}(t)]_{kk}$  ( $k = Z, R$  or  $T$ ) has a maximum of 1, whereas the strongly

decorrelated noise signals (for example, when stations  $A$  and  $B$  are far away) do not show any peak, but show instead a random temporal signal with a variance of  $1/(2T\Delta\omega) \ll 1$  (Sabra *et al.* 2005b; Weaver & Lobkis 2005).

For an omni-directional noise-source distribution, the noise-correlation tensor  $[C_{AB}(t)]_{ij}$  should exhibit the sum of a causal and anticausal contributions that classically correspond to the advanced and retarded Green's function between the two stations. With directive seismic noise as shown in Fig. 2, everything happens as if only one incident plane wave was coherently recorded on the seismic network. The correlation function is thus made of a single causal (or anticausal) coherent signal that should resemble the retarded (or advanced) Green's function if and only if the noise direction is parallel to the station alignment. Fig. 4 presents the obvious case of a noise-correlation tensor that does not match the Green's tensor for surface waves, since signals are still present on transverse components (see  $ZT, TZ, RT$  and  $TR$  in Fig. 4a, red).

*Step 4:* We introduced the ORA as a way to retrieve the surface wave Green's tensor (with both Rayleigh and Love waves) expected from the noise-correlation process in the (0.1–0.2 Hz) frequency bandwidth. For every station pair, the ORA first manipulates the noise-correlation tensor  $[C_{AB}(t)]_{ij}$  by allowing each station to freely turn around both the vertical axis [with the azimuthal angle  $\psi$ , also called the inclination angle (Crampin 1975)] and the radial axis (with the tilt angle  $\beta$ ). For example, considering only rotations performed with azimuthal angles  $\psi_A$  and  $\psi_B$  for

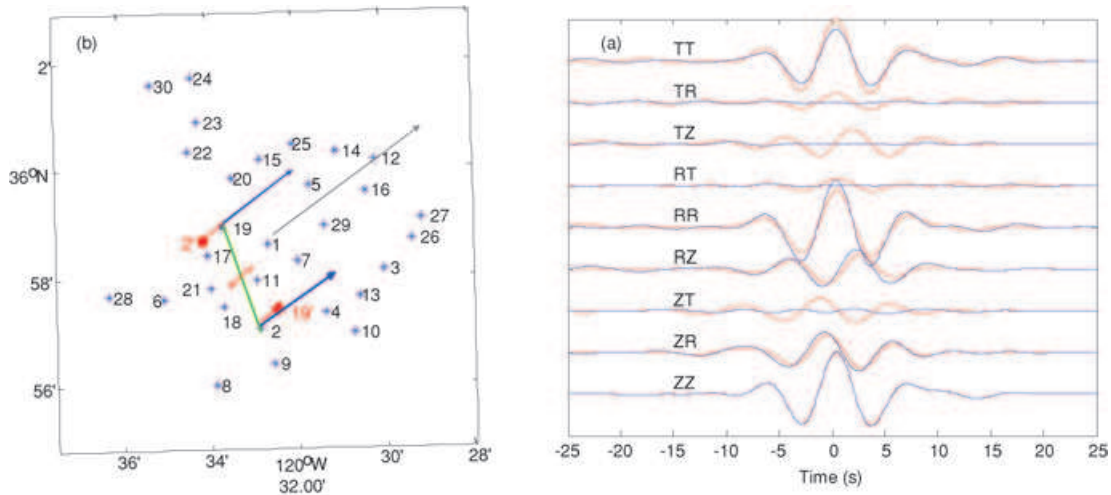


**Figure 4.** Application of the ORA between seismic stations 2 and 19 on Julian day 18. (a) Noise-correlation tensor  $[\tilde{C}_{AB}(t)]_{ij}$  (in red) and optimal noise-correlation tensor  $[\tilde{C}_{AmBm}(t)]_{ij}$  (in blue). (b) Blue arrows show the optimal azimuthal rotation angle  $\psi_m$  to be applied to the two stations. The grey arrow is the incoming noise direction on Julian day 18. After ORA is applied, the optimal correlation tensor describes Rayleigh-wave propagation between station 2 and 19' or between 2' and 19. One can then choose to attribute the optimal noise-correlation tensor to the virtual station pair marked with red crosses.

stations  $A$  and  $B$ , we obtain a new noise-correlation tensor  $[C_{AB}(t)]_{ij}$  such that

$$\begin{aligned} [\tilde{C}_{AB}(t)]_{RR} &= (\cos \psi_A \cos \psi_B)[C_{AB}(t)]_{RR} - (\cos \psi_A \sin \psi_B)[C_{AB}(t)]_{RT} \\ &\quad - (\sin \psi_A \cos \psi_B)[C_{AB}(t)]_{TR} + (\sin \psi_A \sin \psi_B)[C_{AB}(t)]_{TT}. \end{aligned} \quad (3)$$

Similar relationships can be obtained for each component of  $[C_{AB}(t)]_{ij}$  as a function of the angles  $\psi_A$ ,  $\psi_B$  and  $\beta_A$ ,  $\beta_B$ . The second step in the ORA consists of determining the sets of angles,  $\psi_{Am}$ ,  $\psi_{Bm}$ ,  $\beta_{Am}$  and  $\beta_{Bm}$ , that minimize the total energy on the transverse components  $ZT$ ,  $TZ$ ,  $RT$  and  $TR$  of the correlation tensor  $[C_{AB}(t)]_{ij}$ .

For each station pair, the ORA then provides an optimal noise-correlation tensor  $[C_{AmBm}(t)]_{ij}$ , which resembles a surface wave Green's tensor (Fig. 4a, blue) with the Rayleigh wave on the  $ZZ$ ,  $ZR$ ,  $RZ$  and  $RR$  components and a Love wave on the  $TT$  component only.

The optimal azimuthal rotation angles  $\psi_{Am}$  and  $\psi_{Bm}$  are such that each station pair aligns in azimuth with the incident noise direction (peaked around  $\theta_0 \sim 55^\circ$ ). The blue arrows in Fig. 4(b) show  $\psi_{Am}$  and  $\psi_{Bm}$  for seismic stations 2 and 19. The optimal inclination rotations measured by  $\beta_{Am}$  and  $\beta_{Bm}$  are small random numbers between  $-5^\circ$  and  $5^\circ$  as far as minimization results on one-day-long noise correlation measurements can tell. This tilt effect has nearly no contribution on the optimal noise-correlation tensor  $[C_{AmBm}(t)]_{ij}$ . However, we also note that for station pairs with seismometers  $A$  and  $B$  on each side of the SAF, the two optimal azimuth rotation angles  $\psi_{Am}$  and  $\psi_{Bm}$  are slightly different (within  $0$ – $10^\circ$ ). Lateral refraction and ray bending through the SAF is the main reason for these variations. We are not able to draw any conclusions yet for the effects of anisotropy on the azimuth angles  $\psi_{Am}$  and  $\psi_{Bm}$ , but we are pursuing our investigations to see if the ORA measurements can be used for anisotropy inversion.

In conclusion, having  $\psi_{Am}$  and  $\psi_{Bm}$  aligned with the incoming noise direction is the only way to make the noise-correlation tensor match a surface wave Green's tensor. This Green's tensor is associated to a propagation range that is the original distance between stations  $A$  and  $B$  projected on the noise direction  $\theta_0$ .

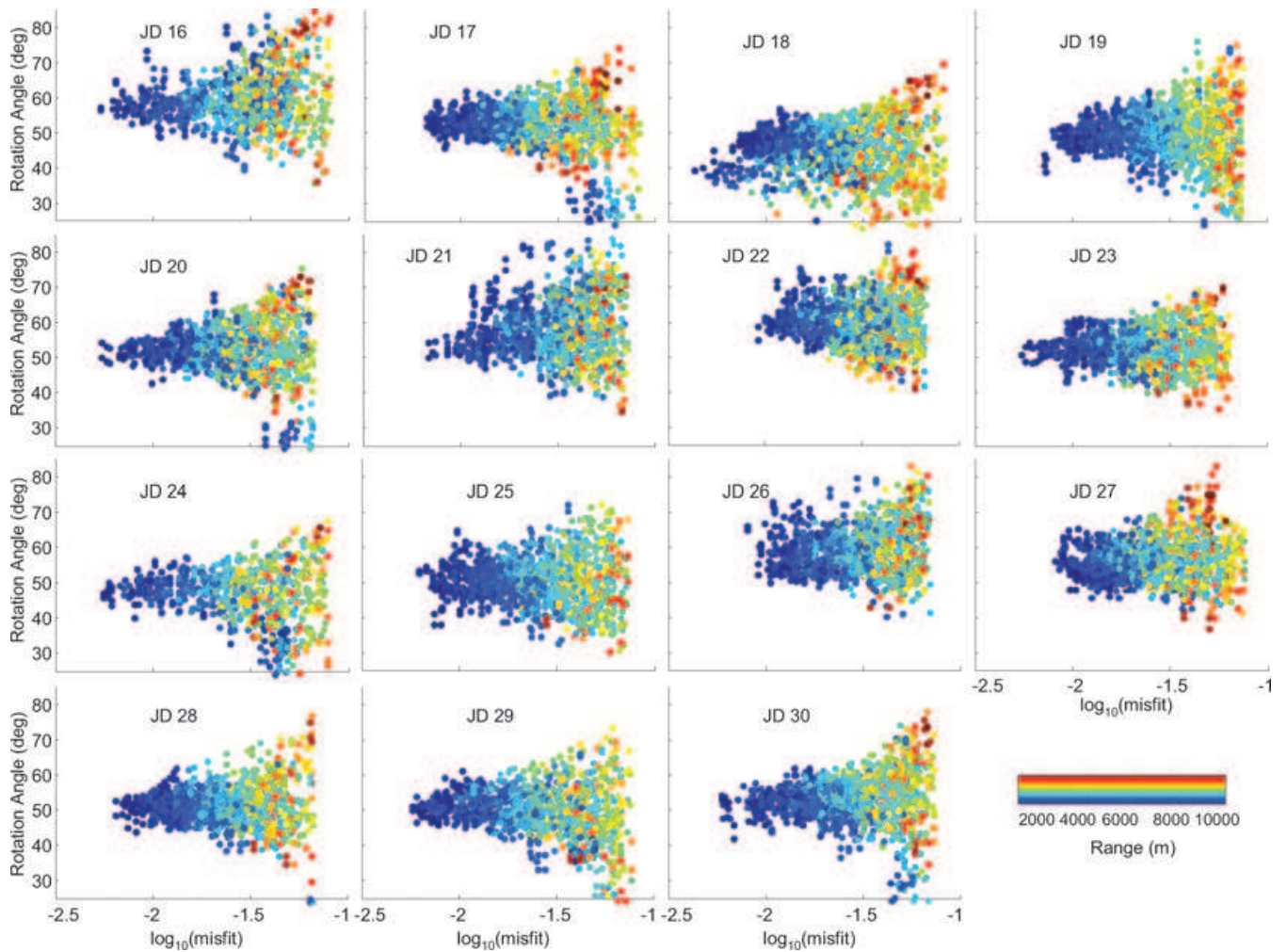
In this approach, we have assumed that both Love and Rayleigh waves were incoming on the seismic network with the same directivity  $\theta_0$ . Note that an algorithm for Love and Rayleigh wave separation from seismic-noise correlation only using intrinsic coherence and polarization filtering has been demonstrated recently (Roueff *et al.* 2009).

Fig. 5 shows the day-by-day evolution of the optimal azimuthal rotation angles  $\psi_m$  plotted as a function of the misfit values for all of the station pairs. Close stations have a better coherence and a smaller misfit. As expected, the average azimuthal rotation angle follows the time evolution of the beamforming output result  $\theta_0$  (Fig. 3a).

*Step 5:* We now use the optimal noise-correlation tensor for surface wave tomography inversion. After ORA is applied, we select all station pairs with a misfit lower than 0.1 to perform tomography. Among the 435 station pairs initially available, this gives a total number of 364 station pairs to be compared to 90 station pairs if only stations in the alignment of the noise direction were selected.

The small size of the seismic network used in this study is both an advantage and a disadvantage regarding tomography inversion: an advantage as the coherence is high for many station pairs, which makes traveltimes measurements very accurate; a disadvantage since traveltimes extracted from the noise-correlation tensor are close to zero, which makes residual uncertainty of great importance in velocity measurement errors. The group velocity measurements were performed through traveltimes picking of the maximum of the envelope of the optimal noise-correlation tensor  $[C_{AmBm}(t)]_{ij}$  on the  $ZZ$  component for the Rayleigh wave and on the  $TT$  component for the Love wave.

Since  $[C_{AmBm}(t)]_{ij}$  corresponds to a surface wave Green's tensor projected along the incoming noise direction, we can define two virtual stations,  $A'$  and  $B'$ , such that  $[C_{AmBm}(t)]_{ij}$  can be associated to propagation between either  $A'$  and  $B'$  or  $A$  and  $B'$  (Fig. 4b). These two paths would be equivalent in a depth-dependent earth model without lateral speed variation, but this is clearly not the case here on the SAF (Bleibinhaus *et al.* 2007). We then make the arbitrary choice to attribute the traveltimes measured from the surface wave tensor  $[C_{AmBm}(t)]_{ij}$  to an effective distance for each station pair, defined as the midpath between  $A$  and  $B$  projected



**Figure 5.** Day-by-day representation of the optimal azimuthal rotation angle  $\psi_m$  versus the optimal rotation misfit for each station pair. Misfit values were calculated as the total energy on components ZT, TZ, RT and TR of the optimal noise-correlation tensor  $[\hat{C}_{AmBm}(t)]_{ij}$  normalized according to the total energy of all of the components. The colour scale corresponds to the range between station pairs.

along the noise direction (Fig. 4a, red crosses). To compensate for potential bias in the tomography inversion, we also introduce a 2.5-km spatial regularization parameter that smoothes out short-scale lateral heterogeneities in the tomography inversion.

Since the incoming noise direction varies from day to day, the effective distance associated to each station pair also varies, which allows the accumulation of spatial and temporal information over the 15 recording days in the area of interest.

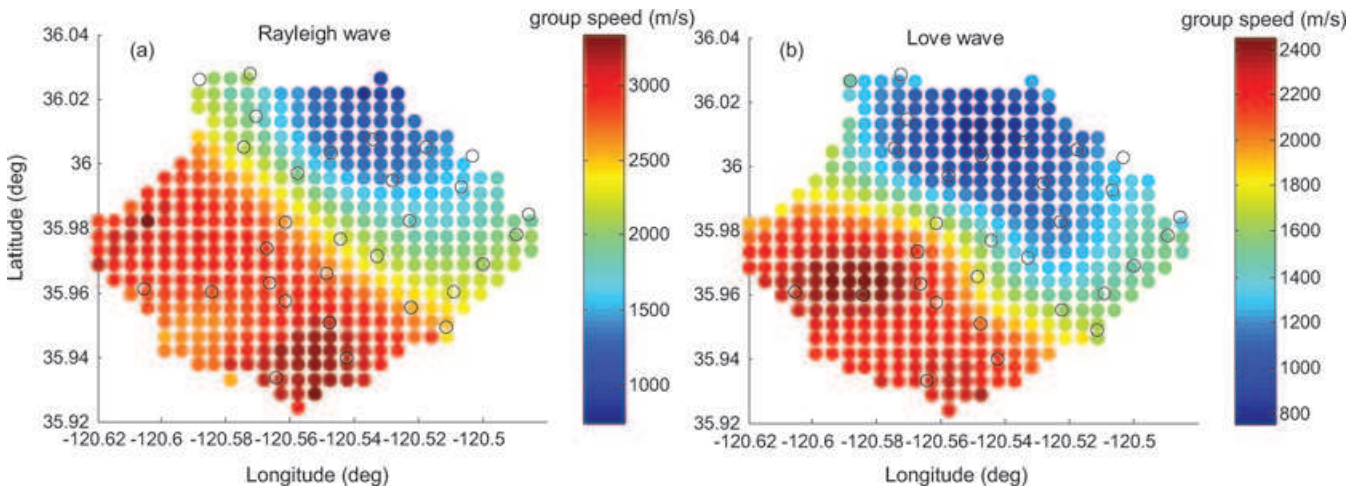
Practically speaking, a simple linear inversion method to construct the tomographic map was used (Tarantola 1987; Menke 1989), assuming straight rays as propagation paths and an *a priori* error covariance matrix that decreases exponentially with distance over five grid cells (Fig. 6). We used a homogeneous starting model based on the *a priori* average regional group velocity  $c_{0R} = 2.6 \text{ km s}^{-1}$  and  $c_{0L} = 2.2 \text{ km s}^{-1}$  for Rayleigh and Love waves, respectively. The inversion is performed on the arrival-time residuals and produces a residual variance reduction of 60 per cent relative to residuals for the homogeneous model.

Fig. 6 shows two group-speed maps for both Rayleigh and Love waves in the (0.1–0.2 Hz) frequency bandwidth obtained through the accumulation of traveltimes measurements extracted from  $[C_{AmBm}(t)]_{ij}$  over 15 consecutive days. The velocity gradient on each side of the SAF is clearly visible. The Rayleigh-wave group

speed maps presented in Fig. 6(a) are in agreement with previous results on a larger scale (Shapiro *et al.* 2005; Moschetti *et al.* 2007). Phase velocities of Love waves are known to be higher than the equivalent Rayleigh waves in the earth crust at long period (above 20 s). However, results are different in seismic exploration at higher frequencies (Gadallah & Fisher 2004). Indeed, Love wave velocity is very sensitive to slow shallow layers (when they exist), when Rayleigh wave velocity is mainly dominated by S-wave velocity. Moreover, Love wave group velocities for a crustal dent structure as observed around the SAF (Bleibinhaus *et al.* 2007) are lower than those for the stratified medium (Yoshida 2000). It is then not surprising to observe group velocities for the Love wave lower than for the Rayleigh wave in the (0.1–0.2 Hz) frequency bandwidth in the Parkfield area.

*Step 6:* The local ellipticity of the Rayleigh wave is another seismic observable that is obtained from the noise-correlation tensor. Ellipticity  $E$  is classically defined as the local ratio of Z/R for a Rayleigh wave issued from a distant source (Tanimoto & Rivera 2005). Fig. 7(a) is the equivalent ZZ/ZR plot issued from the optimal noise-correlation tensor, which confirms the elliptical nature of particle motion for the Rayleigh wave.

Invoking reciprocity relations for elastic waves between stations  $A$  and  $B$ , we can generalize the ellipticity measurement to the



**Figure 6.** Group-speed velocity maps for (a) the Rayleigh wave and (b) the Love wave in the (0.1–0.2 Hz) frequency bandwidth for traveltime information accumulated over 15 consecutive days (Julian days 16–30) and extracted from the optimal noise-correlation tensor  $[\hat{C}_{AmBm}(t)]_{ij}$ . Black circles correspond to station locations.

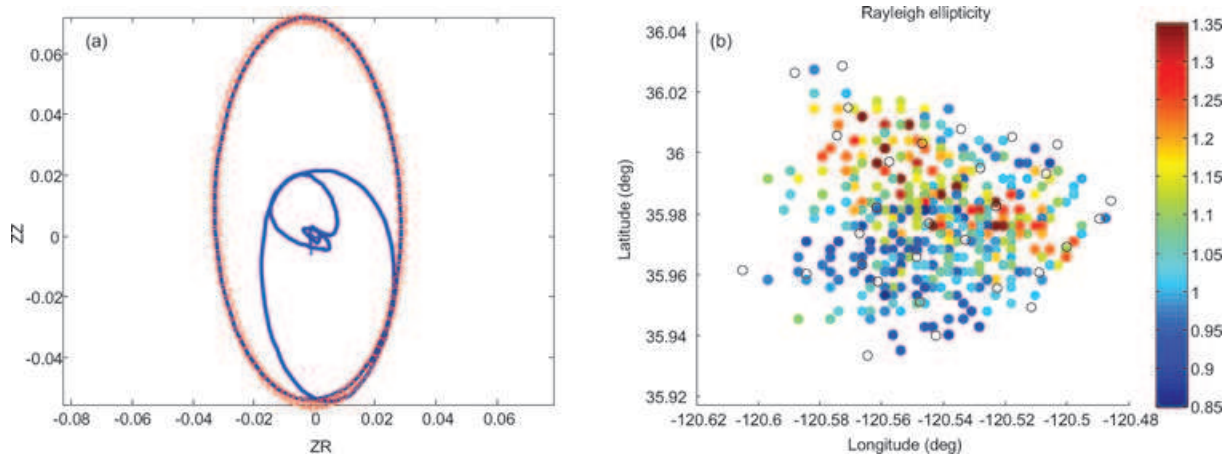


**Figure 7.** (a) Particle motion ZZ versus ZR obtained from the optimal noise-correlation tensor  $[\hat{C}_{AmBm}(t)]_{ij}$  and station pairs 2–19 (see Fig. 4a). The red circles correspond to the best-ellipse fits obtained between  $-5 \text{ s} < t < 5 \text{ s}$ . (b) Average Rayleigh wave ellipticity map in the Parkfield area, California, measured for all of the station pairs on 15 consecutive days (Julian day 16–30). The high values of ellipticity coincide with the SAF. Black circles correspond to station locations.

noise-correlation tensors as:

$$E_A = \frac{Z_A Z_B}{R_A Z_B} = \frac{Z_A R_B}{R_A R_B}, \quad (4)$$

where  $E_A$  is the local ellipticity in station  $A$  and  $Z_A Z_B$  corresponds to the ZZ trace of the optimal noise-correlation tensor  $\hat{C}_{AmBm}(t)$ .

Then, we have:

$$\frac{Z_A Z_B}{R_A R_B} = \frac{Z_A Z_B}{R_A Z_B} \frac{R_A Z_B}{R_A R_B} = \frac{Z_A Z_B}{R_A Z_B} \frac{Z_B R_A}{R_B R_A} = E_B E_A. \quad (5)$$

The maximum of the particle motion ratio ZZ/RR gives the product of the local ellipticity at the two stations  $A$  and  $B$ . The choice to attribute this value as an average ellipticity measurement at the midpoint between  $A$  and  $B$  is arbitrary. From eq. (5), we could theoretically retrieve the local ellipticity in both  $A$  and  $B$  separately, but we prefer to interpret noise correlation as an interferometer that ‘feels’ (or integrates) the whole medium between  $A$  and  $B$ .

Fig. 7(b) shows the average ellipticity map measured over 15 days. The SAF corresponds to high values of ellipticity, as expected from a fractured zone. Ellipticity values away from the SAF are consistent with previous studies (Tanimoto & Alvizuri 2006). Note, however,

that the Rayleigh ellipticity defined through the ZZ/RR ratio of the optimal noise-correlation tensor differs from the classical  $H/Z$  ratio that is directly performed on the recorded noise signals (Tanimoto & Rivera 2005), since ORA separates the contribution of the Love wave from the Rayleigh wave in the ellipticity measurement.

## CONCLUSIONS

In conclusion, we have demonstrated methodological aspects associated with passive seismic tomography in the presence of directive noise. The ORA is defined as a way to retrieve a Rayleigh-Love Green’s tensor from the noise-correlation tensor in the [0.1–0.2 Hz] bandwidth, where surface waves dominate noise recordings. Application to surface wave tomography (including Love and Rayleigh waves) and ellipticity measurements are presented for the SAF in the Parkfield area (CA, USA). The small size of the seismic array contributes to the good quality of the tomography results, since it ensures strong coherence between all station pairs. Another key parameter is the large number of station pairs that are used in the tomography algorithm after ORA is applied.

Future studies will explore: (1) the application of passive seismic techniques to *S*-wave velocity inversion in the crust, through the separate HZ ratios for Rayleigh and Love waves (Tanimoto *et al.* 2006) and (2) the time evolution of the optimal azimuth rotation angles  $\psi_m$  and ellipticity before and after a major seism, to eventually observe anisotropy variation and some opening/closure of cracks in the fault area.

## ACKNOWLEDGMENTS

The authors would like to thank Michel Campillo, Antoine Roueff and Nikolai Shapiro for helpful comments. The facilities of the IRIS Data Management System were used for access to waveforms and the metadata required in this study. The IRIS DMS is funded through the National Science Foundation award EAR-0004370.

## REFERENCES

- Ben-Zion, Y. & Malin, P., 1991. San Andreas Fault zone head waves near Parkfield, California, *Science*, **251**, 1592–1594.
- Bensen, G.D., Ritzwoller, M.H., Barmin, M.P., Levshin, A.L., Lin, F., Moschetti, M.P., Shapiro, N.M. & Yang, Y., 2007. Processing seismic ambient noise data to obtain broad-band surface-wave-dispersion measurements, *Geophys. J. Int.*, **169**, 1239–1260.
- Bleibinhaus, F., Hole, J.A., Ryberg, T. & Fuis, G.S., 2007. Structure of the California Coast Ranges and San Andreas Fault at SAFOD from seismic waveform inversion and reflection imaging, *J. geophys. Res.*, **112**, B06315, doi:10.1029/2006JB004611.
- Brenguier, F., Shapiro, N.M., Campillo, M., Ferrazzini, V., Duputel, Z., Coutant, O. & Nercissian, A., 2008a. Towards forecasting volcanic eruptions using seismic noise, *Nat. Geosci.*, **1**, 126–130.
- Brenguier, F., Campillo, M., Hadziioannou, C., Shapiro, N.M., Nadeau, R.M. & Larose, E., 2008b. Postseismic relaxation along the San Andreas Fault at Parkfield from continuous seismological observations, *Science*, **321**, 1478–1481.
- Catchings, R.D., Rymer, M.J., Goldman, M.R., Hole, J.A., Huggins, R. & Lippus, C., 2002. High resolution seismic velocities and shallow structure of the San Andreas Fault zone at Middle Mountain, Parkfield, California, *Bull. seism. Soc. Am.*, **92**, 2493–2503.
- Campillo, M., 2006. Phase and correlation in ‘random’ seismic fields and the reconstruction of the Green’s function, *Pure. appl. Geophys.*, **163**, 475–502.
- Campillo, M. & Paul, A., 2003. Long-range correlations in the diffuse seismic coda, *Science*, **299**, 547–549.
- Crampin, S., 1975. Distinctive particle motion of surface waves as a diagnostic of anisotropic layering, *Geophys. J. R. astr. Soc.*, **40**, 177–186.
- Gadallah, M.R. & Fisher, R.L., 2004. *Applied Seismology: A Comprehensive Guide to Seismic Theory and Application*, Pennwell Books, Tulsa, OK, USA.
- Gouédard, P. *et al.*, 2008. Cross-correlation of random fields: mathematical approach and applications, *Geophys. Prospect.*, **56**, 375–393.
- Larose, E. *et al.*, 2006. Correlation of random wavefields: an interdisciplinary review, *Geophysics*, **71**, SI11–SI21.
- Menke, W., 1989. *Geophysical Data Analysis: Discrete Inverse Theory*, Academic Press, New York, NY, USA.
- Moschetti, M.P., Ritzwoller, M.H. & Shapiro, N.M., 2007. Surface wave tomography of the western United States from ambient seismic noise: Rayleigh wave group velocity maps, *Geochem. Geophys. Geosyst.*, **8**, Q08010, doi:10.1029/2007GC001655.
- Picozzi, M., Parolai, S., Bindi, D. & Strollo, A., 2009. Characterization of shallow geology by high-frequency seismic noise tomography, *Geophys. J. Int.*, **176**, 164–174.
- Rost, S. & Thomas, C., 2002. Array seismology: methods and applications, *Rev. Geophys.*, **40**, doi:10.1029/2000RG000100.
- Roueff, A., Roux, P. & Réfrégier, P., 2009. Wave separation in ambient seismic noise using intrinsic coherence and polarization filtering, *Signal Process.*, **89**, 410–421.
- Roux, P. & Kuperman, W.A., 2004. Extraction of coherent wavefronts from ocean ambient noise, *J. acoust. Soc. Am.*, **116**, 1995–2003.
- Roux, P., Sabra, K.G., Gerstoft, P. & Kuperman, W.A., 2005. P-waves from cross-correlation of seismic noise, *Geophys. Res. Lett.*, **32**, L19303, doi:10.1029/2005GL023803.
- Sabra, K.G., Gerstoft, P., Roux, P., Kuperman, W.A. & Fehler, M.C., 2005a. Surface-wave tomography from microseisms in southern California, *Geophys. Res. Lett.*, **32**, L14311.
- Sabra, K.G., Roux, P. & Kuperman, W.A., 2005b. Emergence rate of the time-domain Green’s function from the ambient noise cross-correlation function, *J. acoust. Soc. Am.*, **118**, 3524–3531.
- Sánchez-Sesma, F.J. & Campillo, M., 2006. Retrieval of the Green’s function from cross correlation: the canonical elastic problem, *Bull. seism. Soc. Am.*, **96**, 1182–1191.
- Shapiro, N.M., Campillo, M., Stehly, L. & Ritzwoller, M.H., 2005. High resolution surface wave tomography from ambient seismic noise, *Science*, **307**, 1615–1617.
- Tanimoto, T. & Alvizuri, C., 2006. Inversion of the HZ ratio of microseisms for *S*-wave velocity in the crust, *Geophys. J. Int.*, **165**, 323–335.
- Tanimoto, T. & Rivera, L., 2005. Upgrade Rayleigh wave-particle motion, *Geophys. J. Int.*, **162**, 399–405.
- Tanimoto, T., Ishimaru, S. & Alvizuri, C., 2006. Seasonality in particle motion of microseisms, *Geophys. J. Int.*, **166**, 253–266.
- Tarantola, A., 1987. *Inverse Problem Theory*, Elsevier, Amsterdam, the Netherlands.
- Thurber, C., Roecker, S., Zhang, H., Baher, S. & Ellsworth, W., 2004. Fine-scale structure of the San Andreas Fault zone and location of the SAFOD target earthquakes, *Geophys. Res. Lett.*, **31**, L12S02, doi:10.1029/2003GL019398.
- Weaver, R.L. & Lobkis, O.I., 2005. Fluctuations in diffuse field-field correlations and the emergence of the Green’s function in open systems, *J. acoust. Soc. Am.*, **117**, 3432–3439.
- Yang, Y., Ritzwoller, M.H., Levshin, A.L., Shapiro, N.M., 2007. Ambient noise Rayleigh wave tomography across Europe, *Geophys. J. Int.*, **168**, 259–274.
- Yoshida, M., 2000. Fluctuation of group velocity of Love waves across a dent in the continental crust, *Earth Planets Space*, **52**, 393–402.